Nanoscale
Advances

ROYAL SOCIETY
OF CHEMISTRY

PAPER

View Article Online
View Journal | View Issue

Check for updates

Cite this: *Nanoscale Adv.*, 2021, **3**, 847

# Half-Dirac semimetals and the quantum anomalous Hall effect in Kagome $Cd_2N_3$ lattices

Xin-Yang Li, Wei-Xiao Ji, Pei-Ji Wang and Chang-Wen Zhang*

Received 27th June 2020
Accepted 5th December 2020

DOI: 10.1039/d0na00530d

rsc.li/nanoscale-advances

Half-Dirac semimetals (HDSs), which possess 100% spin-polarizations for Dirac materials, are highly desirable for exploring various topological phases of matter as low-dimensionality opens unprecedented opportunities for manipulating the quantum state of low-cost electronic nanodevices. The search for high-temperature HDSs is still a current hotspot and yet challenging experimentally. Herein based on first-principles calculations, we propose the realization of Half Dirac semimetals (HDS) in two-dimensional (2D) Kagome transition-metal nitride $Cd_2N_3$, which is robust against strain engineering. Monte Carlo simulations reveal that $Cd_2N_3$ possesses a Curie temperature reaching up to $T_C = 225$ K, which is much higher than that of the reported monolayers $CrI_3$ ($T_C = 45$ K) and $Cr_2Ge_2Te_6$ ($T_C = 20$ K). The band crossings in $Cd_2N_3$ are gapped out by the spin–orbit coupling, which brings about the quantum anomalous Hall (QAH) effect with a sizeable band gap of $E_g = 4.9$ meV, characterized by the nonzero Chern number ($C = 1$) and chiral edge states. A tight-binding model is further used to clarify the origin of HDSs and nontrivial electronic properties. The results suggest monolayer transition-metal nitrides as a promising platform to explore fascinating physical phenomena associated with novel 2D emergent HDSs and QAH insulators toward realistic spintronics devices, thus stimulating experimental interest.

## 1. Introduction

Spintronics, using an electron's spins instead of its charge to carry information, has attracted extensive attention because of faster transport and dissipation-less properties in magnetic materials.[1,2] To build spintronic devices, the selection of ferromagnetic (FM) materials and control of ferromagnetism, such as the generation and injection of spin-polarized carriers, the manipulation and detection of the spin direction, and the long-distance spin-polarized transport, are crucial and yet challenging. Many concepts of spintronic materials have been put forward to solve these problems, including the use of half-metals (HMs),[3–5] topological insulators (TIs),[6–9] magnetic semiconductors,[10–12] topological nodal line semimetals (TNLSs),[13–15] and so on. Interestingly, two-dimensional (2D) FM ordering has been experimentally discovered in van der Waals crystals $CrI_3$ ($T_C = 45$ K)[16] and $Cr_2Ge_2Te_6$ ($T_C = 20$ K),[17] though their $T_C$ is lower than room temperature, opening the door for the application of 2D spintronics at the nanoscale. Spin-gapless semiconductors (SGS), as shown in Fig. 1(a), possessing a band gap in one of the spin channels while the others keeping a sizeable zero gap in the Fermi level, are more interesting and have been proposed by Wang in 2008.[18] Owing to the special zero band-gap character of SGSs, these types of materials exhibit many novel properties, including (i) only a tiny amount of energy is required to excite electrons from the valence band (VB) to the conduction band (CB); (ii) the excited charge carriers, both electrons and holes, can be 100% spin-polarized simultaneously; (iii) by using the Hall effect, 100% spin-polarized electrons and holes can be easily separated. Many 2D and 3D SGSs,[19–26] including $TMF_3$ (ref. 15) and MX (M = Li, Na, K, Rb, Cs; X = S, Se, Te)[28] exhibit various topological phases. Also, some examples have been synthesized such as $Mn_2CoAl$,[19] and CoFeMnSi.[20] All these provide a new playground and opportunities for spintronic, electronic and optic devices.

Dirac semimetal is a new type of quantum state with non-trivial topological properties. Its body energy band generally has

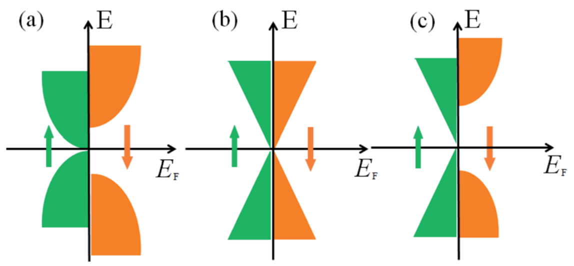

Fig. 1 Schematic rule for designing HDSs. (a) SGSs, (b) Dirac semimetals, and (c) HDSs. The Dirac point of HDSs is exactly located at the Fermi level, unlike that of SGSs. Owing to the intersection of the Dirac-like node and the Fermi level, HDSs represent the real gapless properties rather than half-metals in one spin channel.

---

*School of Physics and Technology, University of Jinan, Jinan, Shandong, 250022, People's Republic of China. E-mail: ss_zhangchw@ujn.edu.cn*

a three-dimensional Dirac point near the Fermi surface. The representative example is monolayer graphene composed of a purely 2D honeycomb network of carbon atoms.[27,29] Low-energy excitation in graphene is governed by $\pi$ electrons in 2p orbitals, whose energy dispersion has linear band crossings with the Dirac-like node at the Fermi level, called the Dirac cones. It exhibits unique electronic properties such as ballistic charge transport,[30] high carrier mobility,[31] and the quantum Hall effect.[32] Subsequently, many 2D lattices such as germanene,[33] carbon allotropes,[34–37] boron allotropes,[38] $SiC_3$,[27] and $C_4N$,[39] have been identified as Dirac materials. However, the Dirac cone in these materials is intrinsically spin-degenerated, which actually limits its utilization in massless spintronics. Thus, the investigation of the controllability of the band crossings and topological phases by using the p-orbital degrees of freedom is desirable, but such an interesting possibility has rarely been investigated.

The ultimate goals for future spintronic devices are to require ultra-fast transport and ultra-lower energy consumption, that is, eliminating the effective mass of electrons or holes and enabling massless charges to be completely spin-polarized. In comparison with parabolic-like SGSs (Fig. 1(a)) and four-degenerated band Dirac cones (Fig. 1(b)), Dirac-like SGSs, termed HDSs, as illustrated in Fig. 1(c), are the better class of magnetic materials for use in spintronic devices as HDSs possess more exotic spin and charge states. Thus, it is highly desirable to find stable HDSs with an intrinsic 100% spin-polarized Dirac state. Normally, HDSs can be divided into two types: type-I, the d-state HDSs, in which the Dirac state is contributed by the d-orbital of transition-metal atoms, and type-II, the p-state HDSs, whose states are from the p-orbital of transition-metal atoms. To date, the majority of reported HDS members belong to type-I HDSs,[39–47] while there has been barely any reports on 2D type-II HDS materials. It is highly desirable to design type-II HDSs with robust spin ordering and a high Curie temperature simultaneously, which may make experimental synthesis largely accessible.

Meanwhile, among the 2D materials family, 2D Kagome lattices have been attracting great interest due to their rich properties. Most members of the family are carbides and oxides (*e.g.*, $Be_3C_2$, $V_2O_3$, $Nb_2O_3$, and LiFeSe),[40–45] consisting of one flat layer with $D_{6h}$ symmetry. Considering that nitrogen has one electron more than the oxygen atom, it is natural to ask whether transition-metal nitrides can also be stabilized in a 2D crystal Kagome lattice. If so, this may open the door to a new family of 2D materials, *i.e.*, 2D Kagome transition-metal nitrides, which will also grow into a big family with fascinating quantum properties.

In this work, we try to address the above challenge and question by proposing a new family of 2D transition-metal nitrides with the Kagome structure. Based on first-principles calculations, we show that $Cd_2N_3$ can be stabilized in this 2D lattice as shown in Fig. 2(a), which is dynamically and thermally stable. Monte Carlo simulations on the basis of the 2D Heisenberg Hamiltonian model show that the Curie temperature $T_C = 225$ K, having potential for high temperature applications. The coexistence of fully spin-polarization and linear dispersion Dirac states can be realized in $Cd_2N_3$, which features ultra-clean energy dispersion and ultra-high Fermi velocity. Distinguished from most proposed nonmagnetic Dirac materials, the four-fold degeneracy neck crossing-point traces out two-fold degeneracy lines emerged in the single-spin channel and the profile of HDSs is revealed by a tight-binding (TB) model. To the best of our knowledge, the $Cd_2N_3$ monolayer represents the first example that hosts the 2D HDS in the equilibrium state. When turning on the spin–orbit coupling (SOC), $Cd_2N_3$ becomes a quantum anomalous Hall (QAH) insulator with its energy gap of $E_g = 5.0$ meV, larger than recently predicted $E_g = 2.3$ meV in Mn-DCA,[38] which is characterized by the nonzero Chern number ($C = 1$) and chiral edge states. In comparison to Cr- or V- doped $(Bi, Sb)_2Te_3$ film,s such a lattice without any magnetic doping is easier to synthesize and has much higher homogeneity. Thus, our discovery not only predicts a family of new 2D HDS materials, which vastly enriches the SGS family, but also provides an experimentally feasible platform to explore the new emergent QAH effect and their fascinating fundamental physical effects.

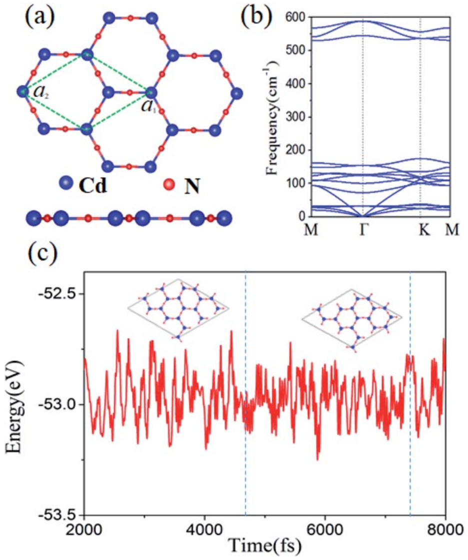

Fig. 2 (a) Top and side views with lattice vectors $a_1$ and $a_2$ in the $x$–$y$ plane. Rhombus shows the unit cell. (b) Calculated phonon spectrum of $Cd_2N_3$. (c) MD simulations at temperature 300 K.

## 2. Computational details and method

All the spin-polarized calculations are performed by using density-functional theory (DFT), as implemented in the Vienna *ab initio* simulation package (VASP).[46] The projector-augmented-wave (PAW) potential,[47,48] Perdew–Burke–Ernzerhof (PBE) exchange-correlation functional[49] and plane-wave basis with a kinetic energy cutoff of 500 eV are employed. An all-electron description, the projector augmented wave method, is used to describe the electron-ion interaction. The Brillouin zone is sampled by using a $9 \times 9 \times 1$ Gamma-centered Monkhorst–Pack grid, and the SOC is included by a second variational procedure on a fully self-consistent basis. During structural optimization, all atomic positions and lattice parameters are fully relaxed, and the maximum force allowed on each atom is less than 0.02 eV $Å^{-1}$. Spin polarization is included through all the calculations. Since standard DFT may fail to describe the magnetism, the Heyd–Scuseria–Ernzerhof (HSE06) functional[54] has been carried out to examine the magnetism and electronic structures. Phonon dispersion is calculated using the finite displacement method, as implemented in the PHONOPY code.[55]

## 3. Results and discussion

Because most elements and compounds are not favorable to directly form a 2D Kagome lattice, we propose a new transition-metal nitride, $Cd_2N_3$, to substitute the Kagome lattice, as illustrated in the top and side views of Fig. 2(a). The $Cd_2N_3$ monolayer forms a honeycomb lattice with a point symmetry of $D_{6h}$ by sharing one nitrogen (N) bridge with each neighbor, reminiscent of the crystal structure in the 2D organic Mn-DCA lattice.[50–53,57,58] The optimized lattice parameters for $Cd_2N_3$ are $a_1 = a_2 = 7.29$ Å, and three N atoms locate around each Cd atom and the bond angle N–Cd–N is 120°, with a Cd–Cd distance of $d = 4.21$ Å. To characterize the thermodynamic stability of $Cd_2N_3$, we calculate the cohesive energy $\Delta E_f$ defined as

$$E_f = E\ (Cd_2N_3) - 2\mu\ (Cd) - 3/2\mu\ (N_2) \tag{1}$$

where $E\ (Cd_2N_3)$ is the total energy, and $\mu$ (Cd) and $\mu(N_2)$ are the chemical potentials taken from bulk Cd and gas phase $N_2$. The calculated result for $Cd_2N_3$ is $E_f = -0.67$ eV per atom, indicating an exothermic chemical reaction. These values are comparable to those of monolayers $CrI_3$ (−0.903 eV per atom)[59] and $Cr_2Ge_2Te_6$ (−0.552 eV per atom).[60] The moderate formation energy also indicates that $Cd_2N_3$ can be realized with a strong bonding network.

It is important to examine whether the experimentally fabricated $Cd_2N_3$ is stable and whether the magnetic state survives at room temperature. To test the kinetic stability of $Cd_2N_3$, we perform phonon spectrum calculations for $Cd_2N_3$, as shown in Fig. 1(b). Apparently, there is no imaginary mode in the whole Brillouin zone, indicating that the $Cd_2N_3$ lattice is dynamically stable. Additionally, the thermal stability of the $Cd_2N_3$ lattice is assessed by performing *ab initio* molecular dynamics (MD) simulations. We use a 4 × 4 supercell to carry out the individual simulations at a temperature of 300 K. As seen from Fig. 2(c), the crystal structure of $Cd_2N_3$ does not collapse throughout 8 ps MD simulation. In fact, Wang *et al*[56] reported that the $Y_2O_3$ lattice forms a complete monolayer on platinum-supported graphene. The $Y_2O_3$ monolayer interacts weakly with graphene, but is stable at high temperature. Scanning tunnelling microscopy reveals that $Y_2O_3$ exhibits a 2D hexagonal lattice rotated by 30° relative to the hexagonal graphene lattice. The above results reveal that the $Cd_2N_3$ monolayer has very good thermal stability and could possibly be prepared in the experiment and survive at room temperature.

We now focus on the magnetic structures of $Cd_2N_3$. Spin-polarized results reveal a spin moment of 5.0 $\mu_B$ per cell as a result of large Hund's rule, which can be further illustrated by spin-polarized electron density, $\Delta\rho = \rho_\uparrow - \rho_\downarrow$, the difference between the electron densities of two spin channels, shown in the inset in Fig. 3(c). A large amount of spins is localized at the N site (∼1.21 $\mu_B$) with a slight contribution from the Cd ion (∼0.08 $\mu_B$), indicating that the N ions mainly contribute to magnetism, also verified by Bader charge analysis.[61] As is known, the Mermin–Wagner theorem[62] reveals that the long-range magnetic ordering is absent by thermal fluctuations in 2D lattices. However, it doesn't hold true for all 2D structures, especially for strong anisotropy cases.[16,17] Thus, to determine the magnetic ground state of $Cd_2N_3$, we consider several possible configurations, including, FM, Neel antiferromagnetic (NAFM), stripe AFM (SAFM), and zigzag AFM (ZAFM), as shown in Fig. 3(a). The calculated results indicate that the FM state ($\Delta E_{FM} = E_{FM} - E_{AFM}$) is energetically 14.43, 12.41, 9.75, and 9.32 meV $N^{-1}$ lower than the NAFM, SAFM, and ZAFM states, respectively. Furthermore, we also check the spin configuration of the coplanar 120° AFM state, and find that the $Cd_2N_3$ monolayer prefers energetically FM ($\Delta E_{FM} = 16.58$ meV $N^{-1}$) states.

Magnetocrystalline anisotropy energy (MAE), defined as the required energy to rotate the magnetization from an easy axis to hard axis of a ferromagnet and determines the difficulty of spin flipping, plays a key role in establishing 2D FM ordering. For a Kagome lattice, MAE ($\theta$, $\varphi$) at an arbitrary direction ($\theta$, $\varphi$) follows

$$\mathrm{MAE}\ (\theta, \varphi) = K_1 \cos^2 \theta + K_2 \cos^4 \theta + K_3 \cos^4 3\varphi \tag{2}$$

where $K_1$ and $K_2$ are system-dependent anisotropy constants and $\varphi$ is the azimuthal angle of rotation. Fig. 3(b) shows MAE ($\theta$, $\varphi$) as a function of the azimuth angle $\theta$ measured from the *out-*

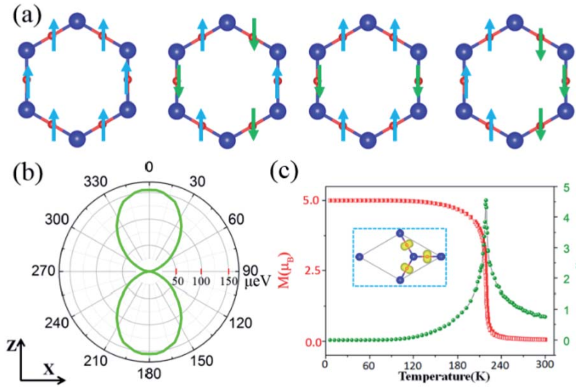

Fig. 3 (a) Possible spin configurations of the Kagome $Cd_2N_3$ lattice: FM, NAFM, SAFM, and ZAFM. (b) Angular dependence of the MAE ($\theta$, $\varphi$) with the direction of magnetization lying on three different planes. The inset illustrates that the spin vector *S* on the *x*–*y*, *y*–*z*, and *x*–*z* planes is rotated with an angle $\theta$ around *x*, *y*, and *z* axis, respectively. (c) MC simulations of the average magnetic moment and spin susceptibility per unit cell with respect to temperature. The electron density of two spin channels for FM spin configuration is defined as 0.001 eV $Å^{-3}$.

*of-plane* axis and the horizontal azimuth angle $\varphi$ on the *in-plane* axis. We find that the energy difference MAE ($\theta$, $\varphi$) is almost independent of *in-plane* azimuthal angle $\varphi$, *i.e.*, $K_3 = 0$, and MAE ($\theta$, $\varphi$) reaches its minimum in the *out-of-plane* axis, indicating an *out-of-plane* magnetization. According to the fits of angular dependence of MAE ($\theta$, $\varphi$), both $K_1$ and $K_2$ are positive with a negligible dependence on $\varphi$, and MAE ($\theta$, $\varphi$) reaches a maximum value of 15 μeV $N^{-1}$ at $\theta_{xz} = \theta_{yz} = \pi/2$, belonging to the family of 2D Ising magnets. Consequently, $Cd_2N_3$ is a 2D Ising magnet, clearly different from the cases of 1*T* – and 2*H*-$VSe_2$ with the *in-plane* magnetization.[63] The *out-of-plane* anisotropy of $Cd_2N_3$ could make the $FM^z$ phase susceptible to thermal fluctuation and correspondingly feasible to realize a 2D magnet at a finite temperature.

The Curie temperature ($T_c$) is a key parameter for the practical application of spintronic devices. Therefore, it is necessary to understand the behavior of magnetism with temperature before implementing $Cd_2N_3$ into practical spintronic devices. On the basis of the 2D Heisenberg model, the spin Hamiltonian can be expressed as

$$H = -\sum_{ij} J_1 S_i S_j - \sum_{ik} J_2 S_i S_k - A S_i^z S_y^z \tag{3}$$

where $J_1$ and $J_2$ are the nearest and next-nearest magnetic exchange interaction parameters, $S_i$ is the spin vector of each atom, $A$ is the anisotropy parameter, and $S^z$ is the $z$ component of the spin vector. A supercell of 100 × 100 with periodic boundary conditions is used here. Fig. 3(c) shows the temperature dependent magnetic moment per unit cell. The magnetic moment begins to drop dramatically at $T_C = 225$ K, implying the formation of the FM state. Additionally, heat capacity ($C_V$) has been calculated, as shown in Fig. 3(c), further confirming the FM-PM phase transition temperature at critical temperature $T_C$. The high $T_C = 225$ K indicates that the $Cd_2N_3$ monolayer may be a promising high-temperature spintronic material.

Having determined the magnetic ground state of the $Cd_2N_3$ monolayer, we present the representative band structures without SOC, as shown in Fig. 4(a), where the blue and red colors display the spin-up and spin-down channels, respectively. One can see that both the spin-up and spin-down channels are completely split away from each other. Remarkably, the spin-up channel possesses a very large band gap 2.88 eV, whereas the spin-down one did not show a gap. Thus the charge transport is dominated by the spin-down electron, and the current flow in such a system should be fully spin-polarized, which is consistent with the case in Fig. 1(a). The band character can be further confirmed by the HSE06 method, which has a larger band gap of 3.56 eV in the spin-up channel. Though the bulk gap is enhanced for HSE06, the HDS bands are not altered near the Fermi level, indicating the robustness of the band character against the computational method. As $E_F$ lies almost in the middle of the spin gap, fully spin-polarized spin-filter efficiency can be maintained in a wide positive or negative bias range, rendering $Cd_2N_3$ an attractive candidate for spin-injection.

The most prominent findings on band dispersion are that in the spin-up channel, there are two several energy band crossings near $E_F$, as shown Fig. 5(a), which mainly originates from the representation of the $D_{6h}$ point group. From the 3D band profile near the K point, accompanied by symmetry analysis, we can obtain the six Dirac-like nodes located exactly at the Fermi level. Notably, this is a typical Kagome band around the Fermi level, consisting of a completely flat band above two Dirac bands remaining at the K point. From the two linear bands in Fig. 5(a), the Fermi velocity $v_F$ of the carriers can be evaluated using linear fitting, $\hbar v_F \approx dE(k)/dk$. The obtained $v_F = 4.3 \times 10^5$ m $s^{-1}$ for $Cd_2N_3$ is comparable to that of graphene ($8.2 \times 10^5$ m $s^{-1}$),[64] and silicene ($5.3 \times 10^5$ m $s^{-1}$).[65] To understand the origin of Dirac states in $Cd_2N_3$, we calculate the orbital-resolved band structures, as shown in Fig. 6. One can see that the wave functions at the Fermi level are mainly from the N-2$p_z$ orbital with a slight contribution from Cd atoms, so there is no $sp^2$ hybridization occurring on $Cd_2N_3$. The linear crossing Dirac states by the N-$p_z$ orbital is consistent with the $p_z$ Dirac state due to the nature of weak π bonds.[66] Namely, $Cd_2N_3$ is a superior candidate of single-spin p-band Dirac materials for high-speed spintronic devices.

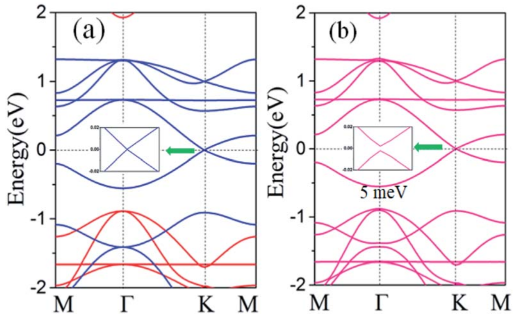

Fig. 4 The energy bands along the high-symmetry lines without (a) and with SOC (b), respectively. The spin-up and spin-down bands are colored in red and blue, respectively. The Fermi level is set to zero.

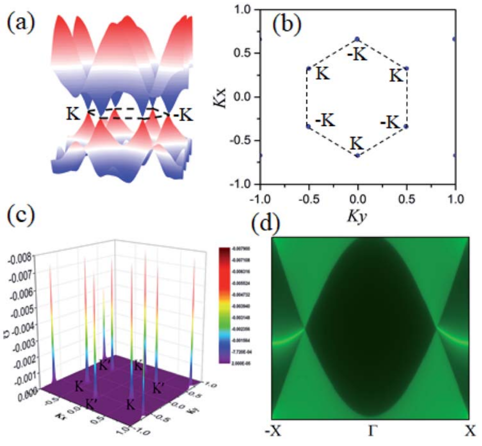

Fig. 5 (a) The calculated 3D energy bands. (b) Berry curvature with SOC in 2D momentum space. The red-white-blue colors give the distribution of Berry curvature from positive to negative values, and the black dashed lines show the first BZ. (c) Distribution of the normalized Berry curvature over the BZ. (d) Chiral edge states of the $Cd_2N_3$ monolayer.

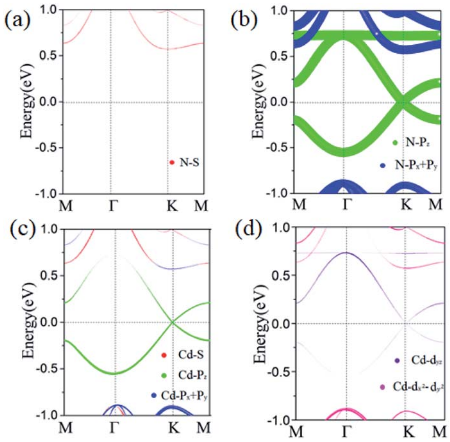

Fig. 6 Orbital-resolved band structures for (a) N-s (b) N-p, (c) Cd-d, and (d) Cd-s states, respectively.

The peculiar band crossings that we found can host topologically nontrivial states in the presence of effective SOC. Fig. 3(b) shows the band structure with SOC, with a gap of $E_g = 5.0$ meV at the Dirac-like node. The band gap is similar to the case of 2D Mn-DCA ($E_g = 2.3$ meV),[44] but smaller than recently predicted $E_g = 20$ meV in $Cs_2Mn_3F_{12}$.[43] It is noteworthy that, due to the small atomic numbers, SOC has negligible effect on the band structure of $Cd_2N_3$. Such band gap opening at the $K$ point suggests a topologically nontrivial feature, which can be confirmed by the Berry curvature $\Omega(k)$ from the Kubo formula[67–69] expressed as

$$\Omega(k) = \sum_n f_n \Omega_n(k) \tag{4}$$

$$\Omega_n(k) = -2\mathrm{Im}\sum_{m\neq n}\frac{\langle\Psi_{nk}|v_x|\Psi_{mk}\rangle\langle\Psi_{mk}|v_y|\Psi_{nk}\rangle\hbar^2}{(E_m - E_n)^2} \tag{5}$$

where the summation is over all of the occupied states, $E_n$ is the eigenvalue of the Bloch function $|\Psi_{nk}\rangle$, $f_n$ is the Fermi-Dirac distribution function, and $v_x$ and $v_y$ are the velocity operators. Fig. 5(b) and (c) show the Berry curvature in the BZ around the $K$ and $K'$ points, which are nonzero with the same sign. By integrating the Berry curvatures over the first BZ, we calculated the Chern number ($C$), expressed as

$$C = \frac{1}{2\pi}\sum_n \int_{\mathrm{BZ}} d^2k\Omega_n. \tag{6}$$

One can see that $C = 1$ with each Dirac cone contributing 0.5, characterizing the topological nature of the gaped state. So the anomalous Hall conductivity $\sigma_{xy}$, $\sigma_{xy} = Ce^2/h$, shows a quantized charge Hall plateau at a value of $e^2/h$ located in the insulating gap of the spin-up Dirac-like node. Such a nonvanishing Chern number $C = 1$ and quantized Hall conductivity in $Cd_2N_3$ characterize the QAH effect.

The two band degeneracy point and the associated band topology can be well modeled by the TB model, taking the $D_{6h}$ lattice symmetry constraint into account. We introduce a Slater–Koster type TB model[73] with the p orbital on the Kagome lattice formed by N atoms. The energy bands near the Dirac points can be expressed by the effective Hamiltonian

$$H = \hbar v_{\mathrm{F}}(k_x\tau_z\sigma_x + k_y\sigma_y) + m_{\mathrm{H}}\sigma_z\tau_z, \tag{7}$$

where $v_{\mathrm{F}}$ is the Fermi velocity, $\sigma_{x,y}$ are the Pauli matrices, $\sigma_z = \pm1$ refers to inequivalent N sublattices, and $\tau_z = \pm1$ refers to the valley pseudo-spin of the $Cd_2N_3$ monolayer. Wave vector $k_{x,y}$ is referenced from $K$ or $K'$.

SOC connects the electron spin and orbital degrees of freedom. So the crystal potential in 2D materials can be approximated by the spherical atomic potential, which gives on-site contribution to the TB Hamiltonian. By averaging the radial degree of freedom, the SOC reads

$$H^{\mathrm{SO}}_{1;\mu,\nu} = \xi_1\left\langle \vec{L}\vec{s}\right\rangle_{\mu,\nu}, \tag{8}$$

where $\vec{s}$ is the vector of the Pauli matrices representing the real spin and $\vec{L}$ is the angular momentum operator. The matrix element $<\cdots>_{\mu,\nu}$ is given on the basis of directed atomic orbitals $\mu$,$\nu$ and $\xi\ell$ is the angular momentum resolved atomic SOC strength with $\ell = \{\mathrm{s,p,d,}\ldots\}$. Obviously, the energy bands are gapped by the effective SOC, which requires nonzero $s_z$ due to its out-of-plane magnetic moment in the $Cd_2N_3$ monolayer. Thus, our TB analysis provides a systematic understanding of the existing first-principles results, and furthermore, a useful guide for further material exploration.

The derived Haldane effective model describes the QAH effect,[70] and the existence of topologically protected chiral edge states is one of the most important signatures of the QAH effect. To reveal the nontrivial topological nature of the $Cd_2N_3$ lattice, we construct Green's functions[71] for the semi-infinite boundary based on the maximally localized Wannier function method.[72,73] Fig. 4(d) shows the local density of states (LDOSs) of the edge states. Obviously, the nontrivial edge states connecting the CB and VB cross the insulating gap of the spin-up Dirac cone, consistent with the Chern number $C = 1$. The spin-polarized Dirac-fermion mediated topological character suggests that the $Cd_2N_3$ monolayer is intrinsic, holding the potential QAH phase.

As is well known, the physical properties of 2D materials can be effectively tuned by strain, like the band gap engineering of 2H-TMD semiconductors.[74] Strain has also been proposed to effectively modulate dielectric properties,[75] SOC,[76] thermal conductivity[77] and interlayer coupling in vdW heterostructures (HTSs)[78] in 2D lattices. In the following, we will show that strain can induce SOC induced bulk gaps and spin-exchange interactions. Fig. 7 presents the evolution of direct gap $E_g$ and FM exchange energy as a function of strain $\varepsilon$, defined as $\varepsilon = (a - a_0)/a_0$, where $a$ ($a_0$) is the strained (equilibrium) lattice constants. Note that the nontrivial topological states remain within the strain range of 10%. This suggests that $Cd_2N_3$ maintains a topologically nontrivial state, which is stable against external strains. The gap $E_g$ decreases slightly with tensile strains, becoming $E_g = 4.95$ meV under strain 10%. Additionally, the variation of total energies of the FM and AFM states ($\Delta E_{\mathrm{FM}} =$

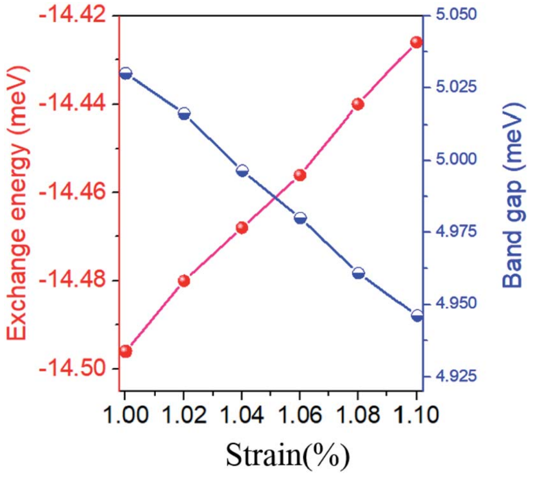

Fig. 7 The variations of the global gap and exchange energy as a function of biaxial strains.

$E_{FM} - E_{AFM}$) with biaxial strains is presented. The results show that the FM ground state of $Cd_2N_3$ is robust against strains. The exchange energy also decreases slightly with increasing tensile strains, for example, when $\varepsilon = 10\%$, $\Delta E_{FM} = 14.43$ meV, leading to less changes of $T_C$. The dependency of $T_C$ onstrain is clearly different from the cases of 2D $FeCl_2$ (ref. [50]) and $CdSe_2$,[51] where $T_C$ changes sensitively with respect to external strains. So we can infer that $Cd_2N_3$ may be a promising intrinsic high-temperature spintronic material. Here we must note that previously proposed strategies to realize p-band FM ordering may be hard to be experimentally controllable, because a strong external electric field or carefully selective doping is required. Our work thus reports the first intrinsic p-band HDS material, even though the experimental synthesis of $Cd_2N_3$ may still remain a challenge. As these magnetic materials potentially offer large spin relaxation times due to small SOC,[79] our results highlight a new promising material for experimental validation studies toward the realistic p-band spintronics applications.

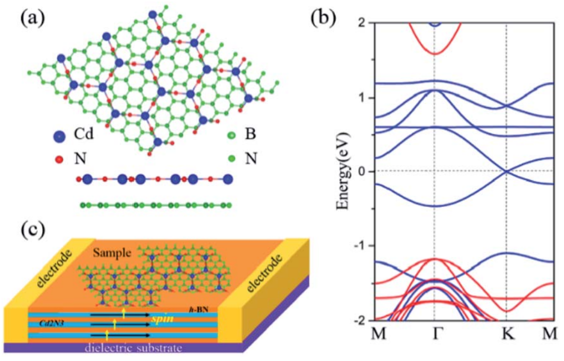

Fig. 8 (a) Top and side views of the epitaxial growth of the $Cd_2N_3$ lattice on the BN substrate. The interlayer distance is 3.10 Å. (b) The corresponding energy band structure of $Cd_2N_3$/BN HTS. (c) Schematic device model for proposed $Cd_2N_3$/h-BN heterostructure for quantum state measurement. Vertical arrows show the spin orientation of electrons in the edge states and horizontal arrows show their transport directions.

Finally, one critical point is whether the QAH effect of 2D $Cd_2N_3$ can remain on a substrate, since the substrates are inevitable in device applications.[80,81] As is known, the BN monolayer is chemically inert and does not easily bond strongly with other atoms, and thus may be adopted as a protective film to grow $Cd_2N_3$. So, the $Cd_2N_3$/BN HTS has been constructed, as shown in Fig. 8(a). Structural optimization indicates that the distance of $Cd_2N_3$ and BN layers is 3.10 Å with a binding energy of −34 meV per unit cell, a typical van der Waals structure. In this case, the main features of the QAH effect in the $Cd_2N_3$ lattice remain intact. Fig. 8(b) presents the calculated band structure with SOC. As expected, here there is still a SOC-induced gap at the Dirac point around the Fermi level, and the states around the Fermi level are dominantly contributed by the Kagome $Cd_2N_3$ band. Given that the 2D BN substrate electrically insulates the adjacent QSH layer of $Cd_2N_3$, protecting parallel helical edge channels from being gapped by interlayer hybridization, $Cd_2N_3$/BN is an ideal HTS to support the dissipationless charge/spin transport in the quantum device. This demonstrates the feasibility of constructing the quantum device with the $Cd_2N_3$/BN heterostructure, as illustrated in Fig. 8(c).

## 4. Conclusion

In summary, we employ first-principles calculations to demonstrate the possibility of realizing HDSs in Kagome lattices with $T_C = 225$ K, which is much higher than that of the reported monolayers $CrI_3$ ($T_C = 45$ K) and $Cr_2Ge_2Te_6$ ($T_C = 20$ K). The inclusion of SOC can turn $Cd_2N_3$ into a QAH insulator, with a sizable band gap of $E_g = 5.0$ meV. Notably, the nontrivial topology is robust against biaxial strain with its band gap reaching up to $E_g = 4.95$ meV under strain 10%. Also, the TB model is constructed to clarify the origin of the HDS and nontrivial electronic properties. Considering that $Cd_2N_3$ enjoys good stability and excellent flexibility, our findings would stimulate further material exploration toward the HDS matter in Kagome materials. These outstanding properties of $Cd_2N_3$ indicate that it is a promising 2D material for potential application in designing energy efficient spintronic devices.

Additionally, the proposed $Cd_2N_3$ is likely to be synthesized by molecular beam epitaxy (MBE) or by the chemical vapor deposition method. We can synthesize $Cd_2N_3$ with a synthesis method similar to that of $Nb_2O_3$.[82] The QAH effect can be probed by scanning probe spectroscopy, ARPES, and ultimately by device fabrications and charge transport measurements. Thus, it offers a new platform for the study of the QAH effect in Kagome lattices for realizing low-dissipation spintronic devices, which is of significant fundamental importance.

## Conflicts of interest

There are no conflicts to declare.

## Acknowledgements

This work was supported by the Taishan Scholar Program of Shandong Province (No. ts20190939), the National Natural

Science Foundation of China (Grant No. 11804116 and 62071200) and the Natural Science Foundation of Shandong Province (No. ZR2018MA033).

## References

1 S. A. Wolf, D. D. Awschalom, R. A. Buhrman, J. M. Daughton, S. von Cdolnár, M. L. Roukes, A. Y. Chtchelkanova and D. M. Treger, *Science*, 2001, **294**, 1488.
2 C. W. Zhang and S. S. Yan, *Appl. Phys. Lett.*, 2009, **95**, 232108.
3 R. A. de Groot, F. M. Mueller, P. G. van Engen and K. H. J. Buschow, *Phys. Rev. Lett.*, 1983, **50**, 2024.
4 H. Van Leuken and R. A. De Groot, *Phys. Rev. Lett.*, 1995, **74**, 1171.
5 K. W. Lee and C. E. Lee, *Adv. Mater.*, 2012, **24**, 2019–2023.
6 D. Hsieh, D. Qian, L. Wray, *et al.*, *Nature*, 2008, **452**, 970.
7 Y. Xia, D. Qian, D. Hsieh, *et al.*, *Nat. Phys.*, 2009, **5**, 398.
8 Y. S. Hor, A. Richardella, P. Roushan, *et al.*, *Phys. Rev. B*, 2009, **79**, 195208.
9 D. Hsieh, Y. Xia, D. Qian, *et al.*, *Phys. Rev. Lett.*, 2009, **103**, 146401.
10 H. Ohno, A. Shen, F. Matsukura, *et al.*, *Appl. Phys. Lett.*, 1996, **69**, 363–365.
11 H. Kimura, T. Fukumura, M. Kawasaki, *et al.*, *Appl. Phys. Lett.*, 2002, **80**, 94–96.
12 A. Ramasubramaniam and D. Naveh, *Phys. Rev. B*, 2013, **87**, 195201.
13 K. Mullen, B. Uchoa and D. T. Glatzhofer, *Phys. Rev. Lett.*, 2015, **115**, 026403.
14 C. Fang, Y. Chen, H.-Y. Kee and L. Fu, *Phys. Rev. B*, 2015, **92**, 081201(R).
15 R. W. Zhang, Z. Zhang, C. C. Liu, *et al.*, *Phys. Rev. Lett.*, 2020, **124**, 016402.
16 B. Huang, G. Clark, E. N. Moratalla, D. R. Klein, R. Cheng, K. L. Seyler, D. Zhong, E. Schmidgall, M. A. Mcguire and D. H. Cobden, *Nature*, 2017, **546**, 270.
17 C. Gong, L. Li, Z. Li, H. Ji, A. Stern, Y. Xia, T. Cao, W. Bao, C. Wang and Y. Wang, *Nature*, 2017, **546**, 265.
18 X. L. Wang, *Phys. Rev. Lett.*, 2008, **100**, 156404.
19 G. D. Liu, X. F. Dai, H. Y. Liu, *et al.*, *Phys. Rev. B*, 2007, **77**, 014424.
20 S. Skaftouros, K. Ozdogan, *et al.*, *Appl. Phys. Lett.*, 2013, **102**, 022402.
21 G. Y. Gao and K. L. Yao, *Appl. Phys. Lett.*, 2013, **103**, 232409.
22 Z. F. Wang, S. Jin and F. Liu, *Phys. Rev. Lett.*, 2013, **111**, 096803.
23 Y. Pan and Z. Yang, *Phys. Rev. B*, 2010, **82**, 195308.
24 L. Bainsla, A. I. Cdallick, M. M. Raja, *et al.*, *Phys. Rev. B*, 2015, **92**, 045201.
25 F. Zheng, C. Zhang, P. Wang, *et al.*, *J. Appl. Phys.*, 2013, **113**, 154302.
26 G. Gao, G. Ding, J. Li, *et al.*, *Nanoscale*, 2016, **8**, 8986–8994.
27 C. L. Kane and E. J. Mele, *Phys. Rev. Lett.*, 2005, **95**, 226801.
28 X. Zhou, R. W. Zhang, Z. Zhang, *et al.*, *J. Phys. Chem. Lett.*, 2019, **10**(11), 3101.
29 A. H. Castro Neto, F. Guinea, N. M. R. Peres, K. S. Novoselov and A. K. Geim, *Rev. Mod. Phys.*, 2009, **81**, 109–162.
30 Y. P. Bliokh, V. Freilikher and F. Nori, *Phys. Rev. B*, 2013, **87**, 2451.
31 K. S. Novoselov, A. K. Geim, S. V. Cdorozov, D. Jiang, M. L. Katsnelson, I. V. Grigorieva, S. V. Dubonos and A. A. Firsov, *Nature*, 2005, **438**, 197–200.
32 Y. Zhang, Y. W. Tan, H. L. Stormer and P. Kim, *Nature*, 2005, **438**, 201–204.
33 S. Cahangirov, M. Topsakal, E. Aktürk, H. Şahin and S. Ciraci, *Phys. Rev. Lett.*, 2009, **102**, 236804.
34 J. Chen, J. Xi, D. Wang and Z. Shuai, *J. Phys. Chem. Lett.*, 2013, **4**, 1443.
35 C. L. Xu, R. Z. Wang, M. S. Miao, X. L. Wei, Y. P. Chen, H. Yan, W. M. Lau, L. M. Liu and Y. M. Ma, *Nanoscale*, 2014, **6**, 1113–1118.
36 Z. Wang, X. F. Zhou, X. Zhang, Q. Zhu, H. Dong, M. Zhao and A. R. Oganov, *Nano Lett.*, 2015, **15**, 6182–6186.
37 H. Zhang, Y. Xie, Z. Zhang, C. Zhong, Y. Li, Z. Chen and Y. Chen, *J. Phys. Chem. Lett.*, 2017, **8**, 1707.
38 X. Qin, Y. Wu, Y. Liu, B. Chi, X. Li, Y. Wang and X. Zhao, *Sci. Rep.*, 2017, **7**, 10546.
39 C. Pu, D. Zhou, Y. Li, H. Liu, Z. Chen, Y. Wang and Y. Ma, *J. Phys. Chem. C*, 2017, **121**, 2669.
40 S. J. Zhang, C. W. Zhang, S. F. Zhang, W. X. Ji, P. Li, P. J. Wang, S. S. Li and S. S. Yan, *Phys. Rev. B*, 2017, **96**, 205433.
41 P. Zhou, Z. S. Mab and L. Z. Sun, *J. Mater. Chem. C*, 2018, **6**, 1206–1214.
42 Y. P. Wang, W. X. Ji, C. W. Zhang, P. Li, P. J. Wang, B. Kong, S. S. Li, S. S. Yan and K. Liang, *Appl. Phys. Lett.*, 2017, **110**, 233107.
43 M. H. Zhang, X. L. Chen, W. X. Ji, P. J. Wang and C. W. Zhang, *Appl. Phys. Lett.*, 2020, **116**, 172105.
44 Y. Y. Deng, Y. Song, Y. Zhang, J. Wang, N. Z. Sun, Z. Yi, Y. Wu, Y. Z. Wu, S. Zhu, J. Wang, J. Chen and X. H. Zhang, *Nature*, 2018, **563**, 94–99.
45 C. Gong, L. Li, Z. Li, H. Ji, A. Stern, Y. Xia, T. Cao, W. Bao, C. Wang, Y. Wang, Z. Q. Qiu, R. J. Cava, S. G. Louie, J. Xia and X. Zhang, *Nature*, 2017, **546**, 265.
46 B. Huang, G. Clark, E. N. Moratalla, D. R. Klein, R. Cheng, K. L. Seyler, D. Zhong, E. Schmidgall, M. A. McGuire, D. H. Cobden, W. Yao, D. Xiao, P. J. Herrero and X. Xu, *Nature*, 2017, **546**, 270.
47 M. H. Zhang, C. W. Zhang, P. J. Wang and S. S. Li, *Nanoscale*, 2018, **10**, 20226.
48 X. J. Ni, W. Jiang, H. Q. Huang, K. H. Jin and F. Liu, *Nanoscale*, 2018, **10**, 11901.
49 L. Zhang, S. F. Zhang, W. X. Ji, C. W. Zhang, P. Li, P. J. Wang, S. S. Li and S. S. Yan, *Nanoscale*, 2018, **10**, 20748.
50 G. Kresse and J. Furthmüller, *Phys. Rev. B*, 1996, **54**, 101169.
51 P. E. Blöchl, Projector augmented-wave method, *Phys. Rev. B*, 1994, **50**, 17953.
52 G. Kresse and D. Joubert, *Phys. Rev. B*, 1999, **59**, 1348.
53 J. P. Perdew, K. Burke and M. Ernzerhof, *Phys. Rev. Lett.*, 1996, **77**, 3865.
54 J. Paier, M. Cdarsman, K. Hummer, G. Kresse, I. C. Gerber and J. G. Ángyán, *J. Chem. Phys.*, 2016, **124**, 154709.
55 A. Togo and I. Tanaka, *Scr. Mater.*, 2015, **108**, 1.

56 Z. F. Wang, Z. Liu and F. Liu, *Nat. Commun.*, 2013, **4**, 1471.

57 X. Zhang, Z. Wang, M. Zhao and F. Liu, *Phys. Rev. B*, 2016, **93**, 165401.

58 R. Addou, A. Dahal and M. Batzill, *Nat. Nanotechnol.*, 2013, **8**, 41.

59 B. Huang, G. Clark, E. Navarro-Moratalla, D. R. Klein, R. Cheng, K. L. Seyler, D. Zhong, E. Schmidgall, M. A. Mcguire and D. H. Cobden, *Nature*, 2017, **546**, 270.

60 C. Gong, L. Li, Z. Li, H. Ji, A. Stern, Y. Xia, T. Cao, W. Bao, C. Wang and Y. Wang, *Nature*, 2017, **546**, 265.

61 G. Henkelman, A. Arnaldsson and H. Jlonsson, *Comput. Mater. Sci.*, 2016, **36**, 354.

62 N. D. Mermin and H. Wangner, *Phys. Rev. Lett.*, 1966, **17**, 1133.

63 M. Esters, R. G. Hennig and D. C. johnson, *Phys. Rev. B*, 2017, **96**, 235147.

64 Y. Jiao, F. Cda, J. Bell, A. Bilic and A. Du, *Angew. Chem.*, 2016, **128**, 10448–10451.

65 Y. L. Wang and Y. Ding, *Solid State Commun.*, 2013, **155**, 6–11.

66 Z. X. Guo, S. Furuya, J. Iwata and A. Oshiyama, *Phys. Rev. B*, 2013, **87**, 235435.

67 Y. G. Yao, L. Kleinman, A. H. MacDonald, J. Sinova, T. Jungwirth, D. S. Wang, E. Wang and Q. Niu, *Phys. Rev. Lett.*, 2004, **92**, 037204.

68 Y. G. Yao and Z. Fang, *Phys. Rev. Lett.*, 2005, **95**, 156601.

69 J. C. Slater and G. F. Koster, *Phys. Rev.*, 1954, **94**, 1498.

70 S. Konschuh, M. Gmitra and J. Fabian, *Phys. Rev. B*, 2010, **82**, 245412.

71 J. L. Lado and J. Fernández-Rossier, *2D Mater.*, 2017, **4**, 035002.

72 C. L. Kane and E. J. Mele, *Phys. Rev. Lett.*, 2005, **95**, 226801.

73 C. C. Liu, W. X. Feng and Y. G. Yao, *Phys. Rev. Lett.*, 2011, **0107**, 076802.

74 P. Johari and V. B. Shenoy, *ACS Nano*, 2012, **6**, 5449.

75 A. Kumar and P. K. Ahluwalia, *Phys. B*, 2013, **419**, 66.

76 P. Koskinen, I. Fampiou and A. Ramasubramaniam, *Phys. Rev. Lett.*, 2014, **112**, 186802.

77 Z. Ding, Q.-X. Pei, J.-W. Jiang and Y.-W. Zhang, *J. Phys. Chem. C*, 2015, **119**, 16358.

78 M. Sharma, A. Kumar, P. K. Ahluwalia and R. Pandey, *J. Appl. Phys.*, 2014, **116**, 063711.

79 S. Sanvito, *Molecular spintronics, Chem. Soc. Rev.*, 2010, **40**, 3336.

80 S. S. Li, W. X. Ji, S. J. Hu, C. W. Zhang and S. S. Yan, *ACS Appl. Mater. Interfaces*, 2017, **9**, 41443.

81 M. Zhou, Z. Liu, W. M. Ming, Z. F. Wang and F. Liu, *Phys. Rev. Lett.*, 2014, **113**, 236802.

82 S. Q. Wang, C. Noguera and M. R. Castell, *Phys. Rev. B*, 2019, **100**, 125408.